



# Intermittent cutting behavior and grinding force model in ultrasonic vibration-assisted grinding K4002 nickel-based superalloy

Yang Cao<sup>1,2</sup> · Biao Zhao<sup>1</sup> · Wenfeng Ding<sup>1</sup> · Jie Wu<sup>2</sup> · Xiaofeng Jia<sup>2</sup> · Jiong Zhang<sup>3</sup> · Raj Das<sup>4</sup>

Received: 27 December 2023 / Accepted: 15 January 2024 / Published online: 7 February 2024  
© The Author(s), under exclusive licence to Springer-Verlag London Ltd., part of Springer Nature 2024

## Abstract

The intermittent cutting behavior, performing as periodic contact phase and separation phase between abrasive grit and workpiece, is an important characteristic in the ultrasonic vibration-assisted grinding (UVAG). This study investigated the effect of intermittent cutting behavior on the grinding force in UVAG. At first, a grinding force model was established by determining the quantity of effective grits and the grinding force of a single grit. Then, the influences of ultrasonic vibration phase on the intermittent cutting behavior and grinding force were discussed. Finally, the prediction accuracy of the model was tested through experiments. Results indicated that the intermittent cutting behavior was divided into the contact phase and separation phase. A large unchanged chip thickness of 1.05  $\mu\text{m}$  was generated at the start of contact phase. The quantity of effective grits firstly increased to maximum 232 at the vibration phase of  $0.5\pi$  and then gradually decreased to zero when entering the separation phase. The maximum error of the grinding force model was 15%, indicating that the model was of high accuracy for the force prediction in UVAG.

**Keywords** Ultrasonic vibration-assisted grinding · Intermittent cutting behavior · Grinding force · Unchanged chip thickness · Quantity of effective grits

## Nomenclature

$A$	Amplitude of ultrasonic vibration
$a_p$	Depth of cut
$B$	Grinding wheel granularity
$C$	Grinding wheel structure number
$D_g$	Diameter of abrasive grit
$E$	Elasticity modulus
$e$	Relative error
$F$	Grinding force
$f$	Frequency of ultrasonic vibration
$F_c$	Total cutting force

$F_{cn}, F_{ct}$	Normal and tangential cutting forces
$F_{dm}$	Shear force exerted from the material
$F_{fg}$	Friction force exerted from the grit
$F_g$	Grinding force of a single grit
$F_n$	Normal grinding force
$F_p$	Total plowing force
$F_{pn}, F_{pt}$	Normal and tangential plowing forces
$F_s$	Total sliding force
$F_{sg}$	Support force exerted from the grit
$F_{sm}$	Support force exerted from material
$F_{sn}, F_{st}$	Normal and tangential sliding forces
$F_t$	Tangential grinding force
$G(z_s)$	Distribution of protrusion height
$h_g$	Unchanged chip thickness
$h_{g(m,n)}$	Unchanged chip thickness of the grit ( $m, n$ )
$h_p$	Height of pile up
$H_s$	Scratch hardness
$h_1, h_2$	Critical unchanged chip thicknesses
$h(l_x)$	Distance between the contour curve and the average line in the position $l_x$
$K_a-K_c$	Constants
$L_a$	Average distance between adjacent abrasive grits
$L_c$	Average contact length of grit

✉ Wenfeng Ding  
dingwf2000@vip.163.com

<sup>1</sup> Jiangsu Key Laboratory of Precision and Micro-Manufacturing Technology, Nanjing University of Aeronautics and Astronautics, Nanjing 210016, China  
<sup>2</sup> Anyang Institute of Technology, School of Mechanical Engineering, Anyang 455000, China  
<sup>3</sup> Department of Mechanical Engineering, College of Engineering, City University of Hong Kong, Kowloon Tong, Kowloon, Hong Kong 999077, China  
<sup>4</sup> Centre for Additive Manufacturing Aerospace Engineering and Aviation, RMIT University, Bundoora 3083, Australia

$N_a$	Total quantity of effective grits
$P_v$	Ultrasonic vibration phase
$Q_a$	Quantity of effective grits
$Q_c$	Quantity of effective grits at the cutting stage
$Q_p$	Quantity of effective grits at the plowing stage
$Q_s$	Quantity of effective grits at the sliding stage
$R$	Radius of grinding wheel
$Ra$	Workpiece surface roughness
$t$	Time
$t_d$	Thickness of the discretized element
$v_s$	Grinding wheel linear velocity
$v_w$	Worktable feed velocity
$x_A, z_A$	Intersection coordinates of the grinding trajectory and the line OE
$x_s, y_s$	Coordinates of grits on the outmost circle surface of grinding wheel
$x_0, y_0, z_0$	World coordinates of grit position at the initial time
$x_1, y_1$	Initial values of grit position
$x_2, y_2, z_2$	Deviation of grit position coordinate
$x_{(m,n)}, z_{(m,n)}$	Coordinates of the target grit in the world coordinate system at time $t$
$z_s$	Protrusion height of grits
$\alpha$	Rake angle of grinding edge
$\beta$	Shear angle
$\dot{\epsilon}_0$	Reference strain rate
$\theta_{\max}$	Maximum contact angle
$\theta_{(m,n)}$	Contact angle of the target grit
$\mu_d$	Mean value of protrusion height
$\mu_s, \mu_p, \mu_c$	Friction coefficients at the sliding, plowing and cutting stages
$\tau$	Shear flow stress
$\sigma_d$	Standard deviation of protrusion height
$\omega$	Grinding wheel angular velocity
$(m,n)$	Number of grits

## 1 Introduction

As promising material, K4002 nickel-based superalloy is widely used in the aviation industry [1–3]. Grinding is an important method for machining of many key parts in the aero-engine, such as disk, shaft, blade, and case [4, 5]. However, large grinding force, severe tool wear, easy ground surface burnout, and low material removal rate commonly occur in the conventional grinding (CG) [6–8], which brings challenges for the high efficiency grinding technology.

Ultrasonic vibration-assisted grinding (UVAG) is a composite machining technology. It combines the ultrasonic vibration and the mechanical cutting [9, 10], making the material removal process under the resonance condition. Wang et al. [11] deemed that the grinding force was

significantly reduced by the elliptical UVAG. The horizontal ultrasonic vibration affected the contact time and unchanged chip thickness, the vertical ultrasonic vibration had influences on the contact length. Zheng et al. [12] deemed that the ultrasonic vibration was helpful in reducing the grinding temperature due to the short contact length, improvement of grit self-sharpening action and low grinding force. Zhou et al. [13] found that a repeated wave-like textures were generated on the workpiece surface because of the overlapping effects of different grinding trajectories in UVAG. The minimum workpiece surface roughness could be obtained with the ideal matching phase difference. According to the abovementioned researches, UVAG has good machining performance for a lot of difficulty-to-cut materials. However, as an important characteristic in UVAG, the influence of intermittent cutting behavior on the grinding force is insufficiently studied.

The grinding force is an important output parameter to evaluate the grindability and it is directly related to the grinding wheel and workpiece material, lubrication condition, and grinding parameters [14–16]. Dai et al. [17] found that the grinding force firstly decreased and then stayed at a steady value of 70% maximum grinding force with an increase in the ultrasonic amplitude, indicating that the minor ultrasonic amplitude performed better than the large amplitude, enabling a small workpiece roughness. Liu et al. [18] established an empirical grinding force model through the multiple regression method. The depth of cut had the most dominant effect on the grinding force, followed by the workpiece feed rate and wheel diameter. Fu et al. [19, 20] studied the single-grain grinding force through the finite element method considering the variation of actual cutting-depth. The largest tensile stress was attained on grain rake face before the actual cutting depth reached the maximum value, indicating that the grit rake face was more easily fractured than the grit tip. Yin et al. [21] proposed an analytical model for UVAG force considering the friction and material deformation. The ultrasonic vibration reduced the relative sliding speed and the friction coefficient on the tool-workpiece interface due to the equivalent softening effect, resulting in the lower friction force. The intermittent cutting behavior reduced the contact length and the cross-sectional area of removed material, which contributed to the lower deformation force. However, the different protrusion height and random position distribution of abrasive grits lead to the ununiformity of unchanged chip thickness in the grinding process. The influence of intermittent cutting behavior on the ununiformity needs to be further analyzed.

The unchanged chip thickness and quantity of effective grits are important factors for revealing material removal mechanism in the grinding. Sun [22] calculated the maximum unchanged chip thickness in UVAG considering the random abrasive grain geometry features. It is found that

the ultrasonic vibration could reduce the grinding force, resulting from the reduction of maximum unchanged chip thickness and fracture toughness. Jamshidi et al. [23] proposed a kinematic-geometrical model to identify the effective number of grits and calculated the dynamic undeformed chip thickness. The percentage of effective abrasive grits increased from 11.5% (on the fresh abrasive wheel surface) to 29.5% (on the worn abrasive wheel surface) with the increase in the operation time of grinding wheel. Hou et al. [24] calculated the number of effective grits considering the Gaussian distribution of abrasive grain size. At most 18% of abrasive grits could contact with the workpiece and 1.79% of the abrasive grains had the cutting effects when the total number of abrasive grains was more than 2 million in the case of conventional grinding wheels. According to the abovementioned researches, the maximum [25], minimum [26], average, and equivalent unchanged chip thicknesses are usually used in the theoretical model of material removal.

The single grit grinding process includes three stages, namely, the sliding, plowing, and cutting according to the different unchanged chip thickness. The macroscopical grinding force is the sum of single grit grinding forces at these three stages. Li et al. [27] found that the contributions of forces at the sliding, plowing, and cutting stages were 65%, 20%, and 15%, respectively, in CG using the electroplated CBN grinding wheel. Wu et al. [28] established a force model based on the infinitesimal method. The frictional coefficient was determined by an additional block-on-ring testing on friction test rig. The error of the force model was 10.37% at most. It can be found that most of the investigations focus on improving the prediction accuracy of grinding force, but few of them discuss the material removal mechanism in UVAG.

The primary goal of this research is to reveal the effect of intermittent cutting behavior in UVAG on the grinding force, which is significant for the optimization of process parameters and improvement of processing efficiency in the grinding of nickel-based superalloy. At first, a theoretical model for the grinding force was established by determining the quantity of effective grits and the grinding force of

a single grit. Subsequently, the parameters used in the force model are obtained through experiments, carefully. Finally, the intermittent cutting is divided into contact phase and separation phase. The influence of intermittent cutting behavior on the unchanged chip thickness and the quantity of effective grits are discussed. The prediction accuracy of the theoretical model is tested.

## 2 Grinding force model development

The following simplifications are often made for modeling the grinding force [29, 30]:

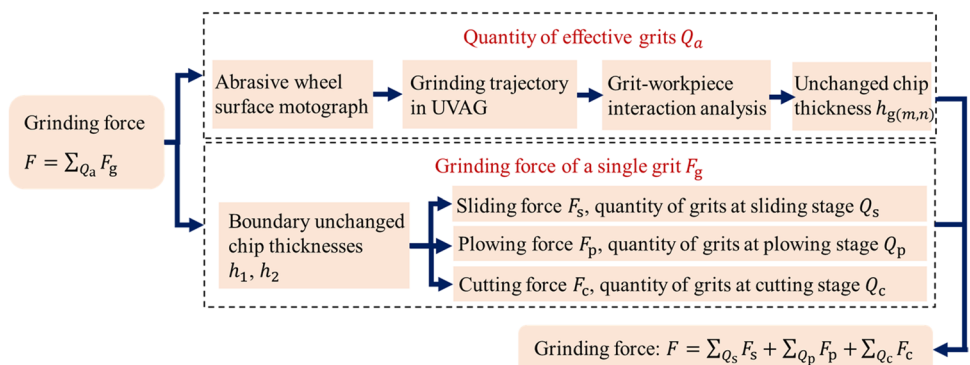
1. All abrasive grits are of same size.
2. The shape of the abrasive grit is conical.
3. The abrasive grits are rigid.
4. The property of workpiece material is uniform.

Additional simplifications will be provided later when they are once used.

Fig. 1 shows the modeling process of the grinding force. On the abrasive wheel surface there are a large number of grits which are the main tool for material removal. The macroscopic grinding force is equal to the sum of all single grit grinding forces, which will be introduced in Section 2.1. Therefore, there are two key parameters, namely the quantity of effective grits and the single grit grinding force in the model. They will be determined in the Sections 2.2 and 2.3, respectively.

The determination of effective grit quantity involves three steps. At first, the topography of abrasive wheel surface is simulated considering the characteristics of grit distribution and the protrusion height. The coordinates of all grits are obtained at initial time. Then, the grinding trajectories of grits in UVAG is calculated, obtaining the coordinates of all grits at any grinding time. Thirdly, the unchanged chip thicknesses of all grits are obtained due to the grit-workpiece interaction analysis through a pass by pass calculation. The quantity of effective grits is obtained.

Fig. 1 Modeling process of the grinding force in UVAG



The determination of single grit grinding force involves four steps. Firstly, the material removal process is divided into the sliding stage, plowing stage and cutting stage according to the unchanged chip thickness. Then, the single grinding forces at these stages are described from Section 2.3.2 to Section 2.3.4. The grinding force can be obtained as the quantity of effective grits and the grinding force of a single grit are known.

## 2.1 Total grinding force

Due to the characteristics of grit random position distribution and nonuniformity protrusion height, not all grits could actually contact to the workpiece surface in the grinding process. Only some outmost grits can cut into the workpiece. These grits are defined as the effective grits. In the case of a single effective grit, a force is generated when the grit cuts into the workpiece and causes the deformation of material. Therefore, the macroscopic grinding force  $F$  can be written as follows:

$$F = \sum_{Q_a} F_g, \quad (1)$$

where  $Q_a$  and  $F_g$  denote the quantity of effective grits and the force of a grit. As key parameters,  $Q_a$  and  $F_g$  will be determined in Section 2.2 and Section 2.3, respectively.

## 2.2 Quantity of effective grits

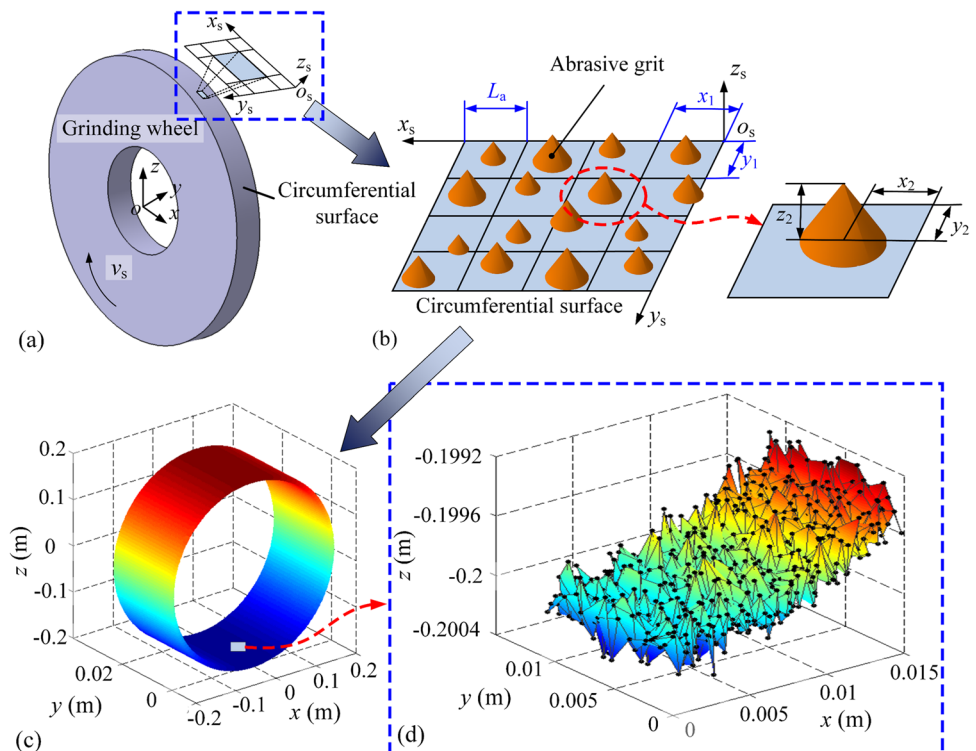
The quantity of effective grits is related to the characteristic of grinding wheel. At first, the grinding wheel surface topography is simulated. Then, the kinematic analysis of grit is carried out considering the grinding trajectory characteristics in UVAG. At last, the unchanged chip thickness of all effective grit is obtained through the analysis on the grit-workpiece geometrical interaction in the grinding zone.

### 2.2.1 Simulation of grinding wheel surface topography

The generation of grinding wheel surface topography is shown in Fig. 2. A local coordinate system  $o_s-x_s y_s z_s$  is established on the circumferential surface of grinding wheel, the  $x_s$ -axis is along the circumference of the grinding wheel. The discretization method [31] is utilized for characterizing the surface topography of grinding wheel. According to the method, the wheel surface is firstly meshed into lots of rectangles. The length of the mesh element is equal to the average distance between adjacent abrasive grits  $L_a$  which is determined by the grinding wheel granularity  $B$  and the grinding wheel structure number  $C$ . According to the Reference [32],  $L_a$  can be expressed as follows:

$$L_a = 137.9B^{-1.4} \sqrt[3]{\frac{\pi}{32-C}}. \quad (2)$$

**Fig. 2** Generation of wheel surface topography. **a** Local coordinates of  $o_s-x_s y_s z_s$  on the circumferential surface of grinding wheel. **b** Distributions of grit position and protrusion height. **c** The simulation of wheel surface topography. **d** The wheel surface topography in the grinding zone



Two important parameters, namely the grit position on the wheel surface and the protrusion height of grit, need to be determined. The information of grit position is represented by the coordinates  $x_s$  and  $y_s$ , while the information of protrusion height is represented by coordinate  $z_s$ . The coordinate values of grit position  $x_s$  and  $y_s$  contain two parts: an initial value and a deviation value. The initial value is the coordinates of the mesh crossing. The deviation value mainly describes the diversity of grits on the grinding wheel surface. Accordingly, the coordinate of a grit ( $x_s, y_s, z_s$ ) can be described as

$$x_s = x_1 + x_2, \tag{3}$$

$$y_s = y_1 + y_2, \tag{4}$$

$$z_s = z_2, \tag{5}$$

where  $x_1$  and  $y_1$  are the initial values of grit position,  $x_1 = iL_a$ ,  $y_1 = jL_a$ ,  $i = 1, 2, 3, \dots, j = 1, 2, 3, \dots, x_2, y_2$ , and  $z_2$  are the deviation values. The deviation value of grit position follows the uniform distribution in the range from 0 to  $L_a$ . The deviation value of protrusion height follows the Gaussian distribution [32, 33]. The distribution of protrusion height  $G(z_s)$  can be written as follows:

$$G(z_s) = \frac{1}{\sigma_d \sqrt{2\pi}} \exp\left(-\frac{z_2 - \mu_d}{2\sigma_d}\right), \tag{6}$$

where  $\mu_d$  and  $\sigma_d$  are the average value and standard deviation of protrusion height,  $\sigma_d = 102 \mu\text{m}$  [34]. In the study, the surface, where the average protrusion height located, is the circumferential surface of grinding wheel. Hence, the value of  $\mu_d$  is equal to zero. According to Eqs. (3)–(5), the abrasive grit in the world coordinates at initial time can be expressed as follows:

$$x_0 = (R + z_s) \sin\left(\frac{x_s}{R}\right), \tag{7}$$

$$y_0 = y_s, \tag{8}$$

$$z_0 = -(R + z_s) \cos\left(\frac{x_s}{R}\right), \tag{9}$$

where  $R$  denote the radius of grinding wheel.

### 2.2.2 Grinding trajectory in UVAG

Fig. 3 shows the grinding trajectory of a single grit. In UVAG, the motion of a grinding edge is composed of wheel rotation, worktable feed motion, and ultrasonic

vibration along the  $x$ -axis. Hence, the coordinate of grit at time  $t$  can be described as

$$x = (R + z_s) \sin\left(\omega t + \frac{x_s}{R}\right) + v_w t + A \sin\left(\frac{2\pi}{f} t\right), \tag{10}$$

$$y = y_s, \tag{11}$$

$$z = -(R + z_s) \cos\left(\omega t + \frac{x_s}{R}\right), \tag{12}$$

where  $v_w$  denotes the worktable feed velocity of grinding machine,  $A$  and  $f$  are the amplitude and frequency of ultrasonic vibration, respectively.  $\omega$  is the grinding wheel angular velocity,  $\omega = v_s/R$ , where  $v_s$  is the grinding wheel linear velocity.

### 2.2.3 Grit-workpiece interaction

In this part, the unchanged chip thickness of all abrasive grits in the grinding zone is calculated one by one in turn, and every abrasive grit is checked whether it is effective or not effective. The transient quantity of effective grits can be obtained by counting all the effective grits at a certain time  $t$ .

According to the discretization method [31], the grinding wheel is discretized along its axial direction ( $y$ -axis in Fig. 2a), as illustrated in Fig. 4a. The thickness of the discretized element  $t_d$  is equal to the average breadth of the microgroove on the ground workpiece surface. The value of  $t_d$  could be obtained by the observation on the topography of workpiece surface using a confocal microscopy, which will be introduced in Section 4.1.

The variables  $(m, n)$  are employed to renumber all abrasive grits on the wheel surface due to the utilization of the discretization method. The variable  $n$  denotes the number of the discretized element,  $n = 1, 2, 3, \dots$ , as illustrate in Fig. 4b. The variable  $m$  represents the serial number of the abrasive grit in the discretized element,  $m = 1, 2, 3, \dots$

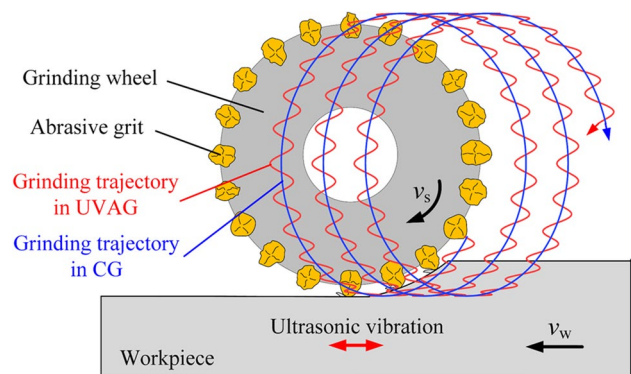
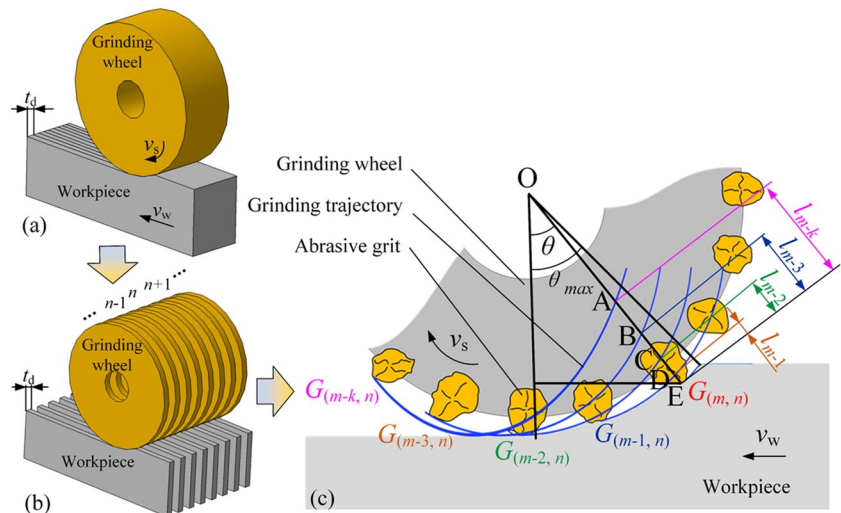


Fig. 3 Illustration of grinding trajectory in UVAG and CG

**Fig. 4** Illustration of grit-workpiece interaction. **a** 3D geometric model of grinding. **b** Discretization model of grinding. **c** Material removal behavior in a piece of discretization element



A random target grit  $G_{(m,n)}$  is selected to be analyzed. Fig. 4 illustrates the material removal process of the target grit. At first, it is determined whether the target grit  $G_{(m,n)}$  is in the grinding zone according to the maximum contact angle  $\theta_{\max}$  and the contact angle of the target grit  $\theta_{(m,n)}$ . They can be expressed as follows:

$$\theta_{\max} = \sqrt{\frac{2a_p}{R}}, \quad (13)$$

$$\theta_{(i,j)} = \omega t + \frac{x_s}{R}, \quad (14)$$

where  $a_p$  is the depth of cut. The target grit is in the grinding zone when the  $\theta_{(m,n)}$  is between zero and  $\theta_{\max}$ . In other cases, the grit is not effective. According to the abovementioned analysis, the unchanged chip thickness of the target grit  $h_{g(m,n)}$  is only related to the grinding trajectories of grit which is in the same discretization element with the target grit  $G_{(m,n)}$ . The unchanged chip thickness of the target grit  $h_{g(m,n)}$  is equal to the minimum values of  $l_{m-1}$ ,  $l_{m-2}$ ,  $l_{m-3}$ ... in Fig. 4c, where the points A–D is the intersection of the grinding trajectory and the line AE. The unchanged chip thickness can be written as

$$h_{g(m,n)} = \min(l_{m-1}, l_{m-2}, l_{m-3} \dots l_{m-k}), \quad (15)$$

$$l_{m-k} = L_{OE} - L_{OA}, \quad (16)$$

where  $L_{OE}$  and  $L_{OA}$  are the length of line OE and OA in Fig. 4c, respectively. According to Eqs. (7)–(9), the coordinates of any grit position at any time can be obtained. Hence,  $L_{OE}$  and  $L_{OA}$  can be described in the following form:

$$L_{OE} = \sqrt{(x_{(m,n)} - v_w t)^2 + z_{(m,n)}^2}, \quad (17)$$

$$L_{OA} = \sqrt{(x_A - v_w t)^2 + z_A^2}, \quad (18)$$

where  $x_{(m,n)}$  and  $z_{(m,n)}$  are the coordinates of target grit in the case of world coordinate system at time  $t$ . These values are obtained according to Eqs. (7)–(9).  $x_A$  and  $z_A$  are the intersection coordinates of the grinding trajectory and the line OE. The values of  $x_A$  and  $z_A$  can be obtained by solving the following equations (19)–(21):

$$\frac{x_A - v_w t}{x_{(m,n)} - v_w t} = \frac{z_A}{z_{(m,n)}}, \quad (19)$$

$$x_A = (R + z_{s(m-k,n)}) \sin \left( \omega t_{(m-k,n)} + \frac{x_{s(m-k,n)}}{R} \right) + v_w t_{(m-k,n)} + A \sin \left( \frac{2\pi}{f} t_{(m-k,n)} \right), \quad (20)$$

$$z_A = -(R + z_{s(m-k,n)}) \cos \left( \omega t_{(m-k,n)} + \frac{x_{s(m-k,n)}}{R} \right), \quad (21)$$

where  $t_{(m-k,n)}$  is the time parameter,  $t - 2\pi/\omega \leq t_{(m-k,n)} \leq t$ . In these equations, Eq. (19) describes the line OE, and Eqs. (20) and (21) describe the grinding trajectory of the grit  $G_{(m-k,n)}$ . According to Eqs. (15)–(21), the unchanged chip thickness of the target grit could be obtained. The target grit is effective when the unchanged chip thickness is a positive value. Afterwards, the unchanged chip thickness of the next grit will be obtained using the same calculation step. Finally, the number of effective grits is known as the unchanged chip thicknesses of all abrasive grits in the grinding zone are obtained. In the research, ten different grinding wheels with random surface topography is generated and analyzed according to the discretization method. In terms of one grinding wheel, the data for continuous grinding for 0.05 s using same grinding parameters are recorded with the

resolution of 0.002 s. The distribution of unchanged chip thickness is obtained by averaging the results of all abrasive wheels.

### 2.3 Grinding force of a single grit

Generally, the material removal process is divided into the sliding stage, plowing stage, and cutting stage. The boundaries of these stages are related to the value of unchanged chip thickness. Firstly, the boundary unchanged chip thicknesses of these three stages are obtained. Then, the expressions of sliding force, plowing force, and cutting force are determined.

#### 2.3.1 Three stages in the material removal process

According to unchanged chip thickness [35–37], the grinding force of a single grit is divided into the sliding force, plowing force and cutting force. The grinding force can be written as

$$F_n = F_{sn}Q_s + F_{pn}Q_p + F_{cn}Q_c, \tag{22}$$

$$F_t = F_{st}Q_s + F_{pt}Q_p + F_{ct}Q_c \tag{23}$$

where  $F_n$  and  $F_t$  are the normal and tangential grinding forces, respectively;  $F_{sn}$ ,  $F_{st}$  are the normal and tangential sliding forces, respectively;  $F_{pn}$ ,  $F_{pt}$  are the normal and tangential plowing forces, respectively;  $F_{cn}$ ,  $F_{ct}$  are the normal and tangential cutting forces, respectively; and  $Q_s$ ,  $Q_p$ , and  $Q_c$  are the numbers of abrasive grits at the sliding stage, plowing stage, and cutting stage, respectively. The boundaries unchanged chip thickness of these three stages are illustrated in Fig. 5. The material performs elastic deformation when unchanged chip thickness is smaller than  $h_1$ . The plastic deformation occurs when unchanged chip thickness is larger than  $h_1$  but smaller than  $h_2$ . The material could be pushed to the side of the abrasive grit or compressed under the abrasive grit. The fracture occurs in the workpiece material due to the severe plastic deformation when the unchanged chip thickness exceeds  $h_2$ . The chip is generated in front of abrasive grit. In the research, the values of  $h_1$  and  $h_2$  are determined using the two-dimension slip-line model [38] which considers the property of workpiece material, the size of abrasive grit, the cooling and lubrication. The boundary unchanged chip thickness of these three stages can be described as

$$h_1 = 0.5K_aD_g \left( 1 - \sqrt{\frac{1}{1 + \tan^2(0.5\cos^{-1}(K_b))}} \right), \tag{24}$$

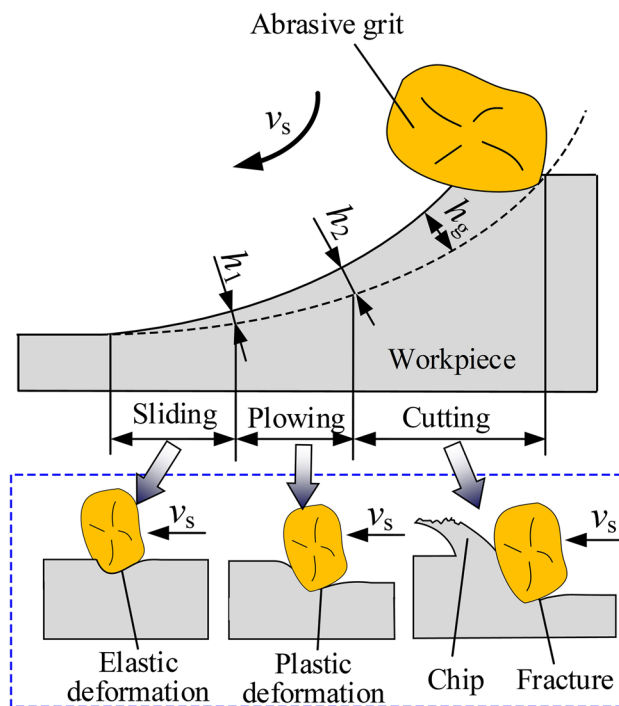


Fig. 5 Three stages in the material removal behavior of a single grit

$$h_2 = 0.5K_aD_g \left( 1 - \sqrt{\frac{1}{1 + \tan^2(0.25\pi - 0.25\cos^{-1}(K_b))}} \right), \tag{25}$$

where  $K_a$ ,  $K_b$ , and  $D_g$  denote material property parameter, the interfacial friction parameter, and the diameter of abrasive grit, respectively,  $D_g = 68B^{-1.4}$  [13],  $K_b = 0.55$  [38]. The values of  $Q_s$ ,  $Q_p$ , and  $Q_c$  are obtained, as the boundary unchanged chip thickness and the unchanged chip thickness of all effective grit are known.

#### 2.3.2 Grinding force at the sliding stage

Due to the small undeformed chip thickness, the sliding force is caused by the material elastic deformation and the friction. According to the Hertzian contact model [38–40], the sliding forces are written as follows:

$$F_{sn} = \frac{4}{3}E \left( \frac{D_g}{2} \right)^{\frac{1}{2}} (h_g)^{\frac{3}{2}}, \tag{26}$$

$$F_{st} = \mu_s F_{sn}, \tag{27}$$

where  $\mu_s$  denote the friction coefficient, and  $E$  denotes the elasticity modulus.

### 2.3.3 Grinding force at the plowing stage

With the increase in the unchanged chip thickness, the workpiece material cannot recover when the abrasive grit passes through the material. The pile up of workpiece material is formed on the side of abrasive grit due to the plastic deformation. According to the upper bound model [35, 41, 42], the plowing force can be written as follows:

$$F_{pn} = H_s h_g (h_g + h_p) \tan^2 \alpha, \tag{28}$$

$$F_{pt} = \mu_p F_{pn}, \tag{29}$$

where  $h_p$  is the height of pile up in single-grain cutting,  $(h_g + h_p) = K_c D_g / (2 \tan \alpha)$ ,  $\alpha$  denotes the rake angle of grinding edge,  $K_c$  is a constant, and  $\mu_p$  denotes the friction coefficient at the plowing stage. According to the theoretical analysis of plane stain [35, 41], for a rigid perfectly plastic body, the scratch hardness  $H_s$  approximately equals to the static hardness of material.

### 2.3.4 Grinding force at the cutting stage

At the cutting stages, Ozlu et al. [43] proposed a simplification that the shear stress is only uniformly distributed on the shear plane, and no plastic deformation occurs before and after the shear plane on the rake face. According to the simplification, the force analysis in the material removal process is illustrated in Fig. 6. The region  $S$  is subjected to the combined four forces, including the support force exerted from the grit  $F_{sg}$  and the support force exerted from material under the region  $F_{sm}$ , the friction force exerted from the grit  $F_{fg}$ , and the shear deformation force exerted from the material  $F_{dm}$ . The directions of the four forces are shown in Fig. 6. Under the combined forces, the region  $S$  moves along the shear plane at a constant velocity. Therefore, these four forces can be broken down into the forces along the horizontal and vertical directions. The equation of mechanics is established as follows:

$$F_{sg} \cos \alpha = F_{dm} \sin \alpha + F_{sm} \sin \beta + F_{fm} \cos \beta, \tag{30}$$

$$F_{sm} \cos \beta = F_{sg} \sin \alpha + F_{dm} \cos \alpha + F_{fm} \sin \beta, \tag{31}$$

where  $\beta$  denotes the shear angle.

The friction force and the shear force can be written as [44–46]

$$F_{fg} = \mu_c F_{sg}, \tag{32}$$

$$F_{dm} = \tau \frac{h_g}{\sin \beta}, \tag{33}$$

$$\beta = 0.25\pi - 0.5(\alpha + \arctan(\mu_c)), \tag{34}$$

where  $\tau$  is the shear flow stress, and  $\mu_c$  is the friction coefficient. According to Ref. [27], the shear flow stress can be described as follows:

$$\tau = K_d \ln \left( \frac{K_e v_s \cos \alpha \sin \beta}{h_g \cos(\alpha + \beta) \dot{\epsilon}_0} \right), \tag{35}$$

where  $K_d$  and  $K_e$  are the constants, and  $\dot{\epsilon}_0$  denotes the reference strain rate,  $K_e = 10$  [27, 47, 48].

According to Eqs. (30) and (31), the support forces can be obtained as follows:

$$F_{sw} = F_{dm} \tan(\alpha + \beta) + F_{fg} \cos^{-1}(\alpha + \beta), \tag{36}$$

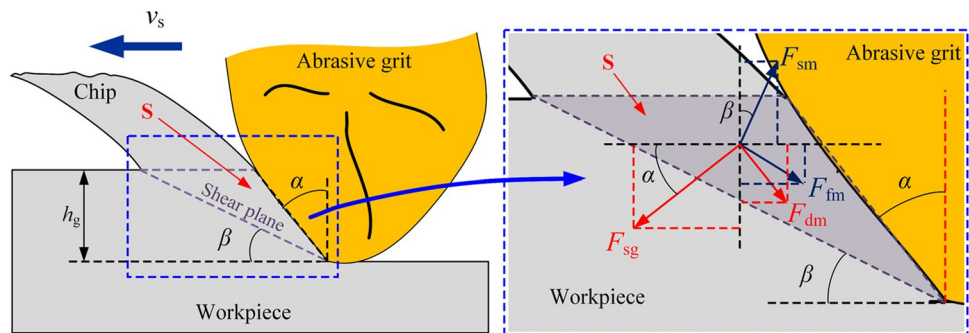
$$F_{sg} = F_{dm} \cos^{-1}(\alpha + \beta) + F_{fg} \tan(\alpha + \beta). \tag{37}$$

According to Eqs. (30), (31), (36), and (37), the normal and tangential forces of a single grit can be written as

$$F_{cn} = \frac{\pi}{2} \tau h_g^2 \tan \alpha \left( \frac{\sin \alpha \cos \alpha}{\cos \beta \cos(\alpha + \beta)} + (\tan(\alpha + \beta) \sin \alpha + \cos \alpha) \mu_c \right), \tag{38}$$

$$F_{ct} = \frac{\pi}{2} \tau h_g^2 \tan \alpha \left( \frac{\cos^2 \alpha}{\cos \beta \cos(\alpha + \beta)} + (\tan(\alpha + \beta) \cos \beta - \sin \alpha) \mu_c \right). \tag{39}$$

Fig. 6 Illustration of force analysis at the cutting stage





As the number of effective grits at three stages and the grinding force of single grit are described, the normal and tangential grinding forces can be obtained in Eqs. (22) and (23).

### 3 Experimental setup

The UVAG experiment was finished on a grinding machine (Profimat MT-408, BLOHM, Germany), as shown in Fig. 7. The ultrasonic generator produced the electrical signals. Then, the ultrasonic transducer converted the electrical signals to the high frequency mechanical vibration [49, 50]. The horn focused the acoustic energy on the small front face, enabling an increase in the vibration amplitude. The workpiece made of K4002 nickel-based superalloy was fixed on the ultrasonic sonotrode surface. The length, width, and thickness of workpiece were 20 mm, 18 mm, and 12 mm, respectively. Corundum abrasive wheels (code, WA80F8V35m/s) in the size of 400 mm (external diameter)  $\times$  178 mm (inner diameter)  $\times$  20 mm (thickness) were employed in the experiments. The grinding wheel was dressed by a dresser pen with the dressing velocity of 20 m/s and the axial feed velocity of 100 mm/min. The total dressing amount was 0.2 mm, and the amount of dressing per axial feed was 0.01 mm. A waterproof plate was used in the ultrasonic vibration system. The experimental parameters are listed in Table 1.

Before the experiments, the impedance characteristic of the ultrasonic sonotrode was tested by the Impedance analyzer (PV50A, Banglianshidai, China). Then, the relationship between the amplitude of ultrasonic vibration and the output power was calibrate using the laser vibrometer (SOP-TOPS LV-S01, Sunny, China). The resonant frequency of ultrasonic sonotrode with the workpiece was 19.3 kHz. The minimum dynamic resistance was 16.3  $\Omega$ , suggesting that the ultrasonic sonotrode worked well in resonance.

The grinding force was measured using the dynamometer (9253B, Kistler, Switzerland) which was installed under

**Table 1** Experimental grinding parameters

Parameter	Value
Grinding mode	Down-grinding
Ultrasonic frequency $f$ (kHz)	19.3
Ultrasonic amplitude $A$ ( $\mu\text{m}$ )	0, 1, 3, 5, 7
Depth of cut $a_p$ (mm)	0.1, 0.3, 0.5
Worktable feed velocity $v_w$ (mm/min)	150, 250, 350
Grinding velocity $v_s$ (m/s)	20, 25, 35

the ultrasonic sonotrode and above the machine worktable. The force signals were then processed by the signal amplifier (5080A, Kistler, Switzerland). At present, the average value of force signals at the stable grinding stage was usually regarded as the grinding force in UVAG because the dynamic force was hard to be completely collected by the dynamometer with a smaller sampling frequency than the ultrasonic vibration [11]. Therefore, a low-pass filter was utilized with the cutoff frequency of 5 Hz. The average values of force signals at the stable grinding stage were records as the grinding force.

The topography of the ground workpiece surface and the grinding wheel surface was observed through a three-dimensional confocal microscope (S Neox, Sensofar, Spain). The surface roughness was measured by a roughness meter (MarSurf PS1, Mahr, Germany). Five regions on the surface of each workpiece were measured using the roughness meter. The sampling length and evaluation length for surface roughness were 0.8 mm and 4 mm, respectively. The measurement direction was perpendicular to the grinding direction. The final value was obtained by averaging the data.

The experimental process was divided into the pre-experiments and the validation experiments. In the pre-experiments, seven groups of grinding tests were conducted. Each group consists of three grindings using same processing parameters. The final force was equal to the average value of these three grindings. The constants in the theoretical force model were determined through fitting the results from these

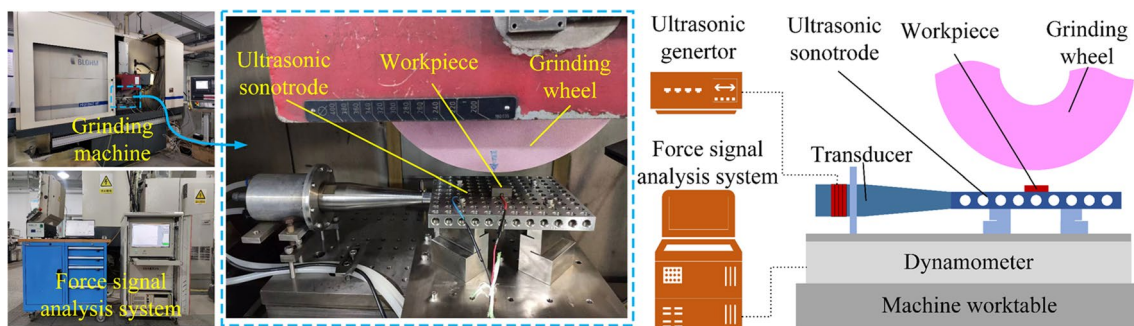


**Fig. 7** Experiment setup

grinding tests. In the validation experiments, the prediction accuracy was tested by other grinding tests. The evaluation of the theoretical force model was obtained according to the experimental results.

## 4 Results and discussion

### 4.1 Parameters determination in the force model

This section mainly introduces the determining method of the parameters in the theoretical force model. In the grinding, the topography of workpiece surface is formed by larger number of abrasive grits [51]; therefore, the vertex angle of the grit  $2\alpha$  in the model was obtained through the observation on the surface topography, as illustrated in the Fig. 8. For every ground workpiece surface, nine random regions were selected to be observed in the study. It can be found that the contour curve of surface along the  $x$ -axis (grinding direction) is very flat in CG, but the contour curve along the  $y$ -axis is rough. A lot of long grinding traces is parallel-distributed on the workpiece surface, resulting from the

continuous contact behavior of a grit. The contour curve of grinding traces along the  $y$ -axis is displayed in Fig. 8a. The angel between the sides of the grinding traces changes in a small range from  $164^\circ$  to  $170^\circ$ . The average value is approximately  $167^\circ$ . Fig. 8b displays the topography of workpiece surface in UVAG. The contour curves along the  $x$  and  $y$  directions are both jagged due to the intermittent cutting behaviors in UVAG. Hence, the grinding traces are short and periodically distributed. The angle between the sides of grinding trace is very close to the results in CG.

The thickness of the discretized element  $t_d$  is obtained according to the workpiece surface roughness. Fig. 9 shows the relationship between grinding parameters and the workpiece surface roughness  $Ra$ . In general, the value of  $Ra$  is increased with the increase in the worktable feed velocity and grinding velocity; the value of  $Ra$  in UVAG is smaller than that in CG. But, the difference in CG and UVAG is not significant in all experimental results. The maximum value of the difference is 8%. In addition, the workpiece surface roughness in all experimental results changes in a small range from 0.47 to 0.75  $\mu\text{m}$ . Fig. 10 illustrates the contour curve of workpiece surface along the  $y$ -axis.  $Ra$  is equal to

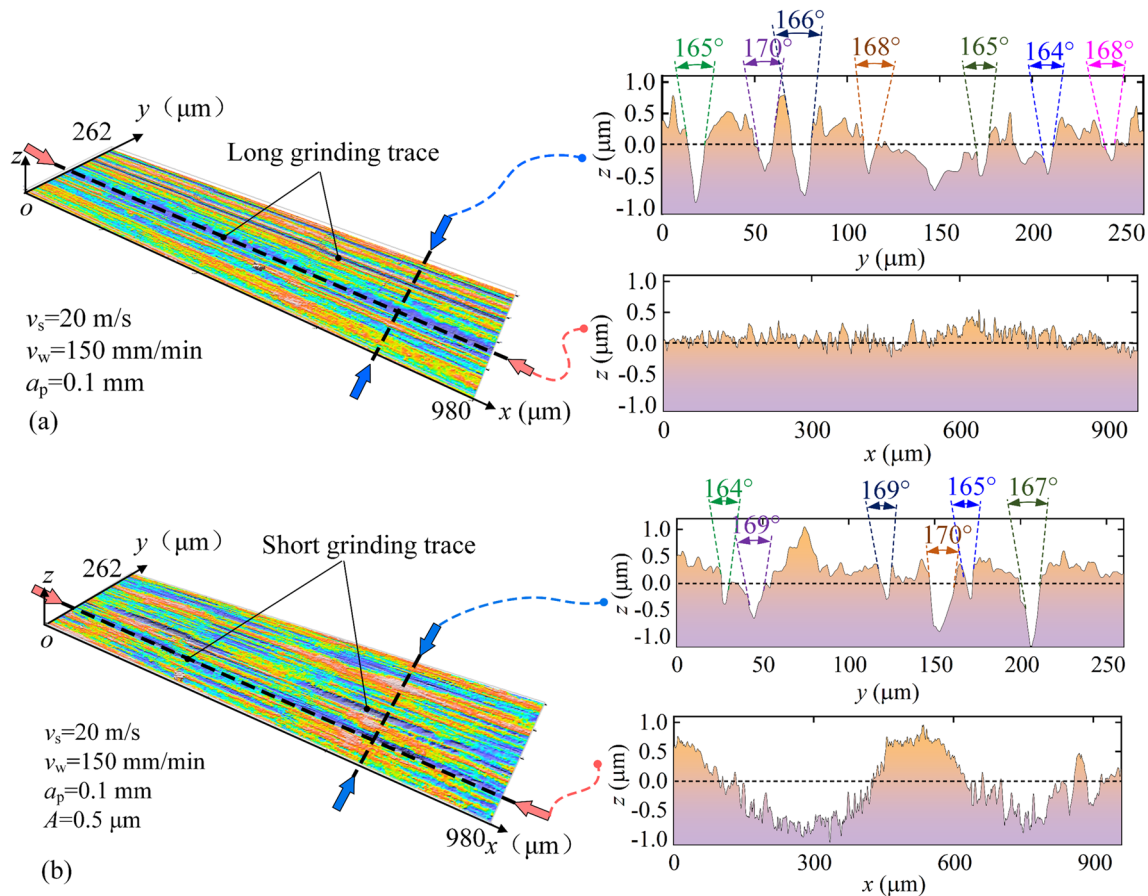


**Fig. 8** Workpiece surface topography **a** in CG and **b** in UVAG

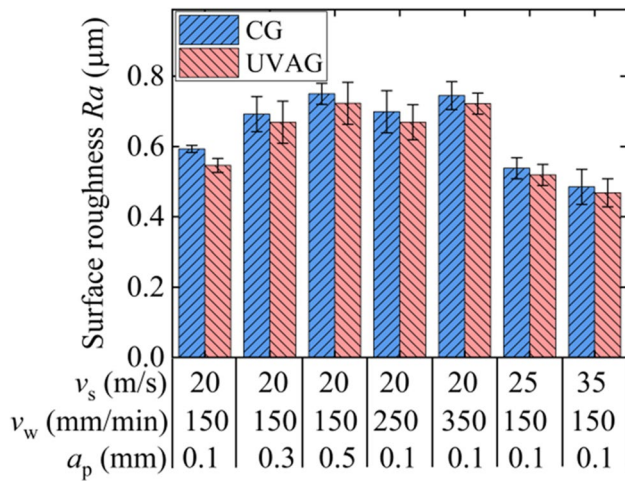


Fig. 9 Workpiece surface roughness in CG and UVAG

the average contour deviation. According to the deification, the relationship between the thickness of the discretized element  $t_d$  and the workpiece surface roughness  $Ra$  can be written as follows:

$$Ra = \frac{1}{L} \int_L |h(l_x)| dl_x = \frac{1}{8} t_d \cot \frac{\alpha}{2}, \tag{40}$$

where  $h(l_x)$  denotes the distance between the contour curve and the average line in the position  $l_x$ , as shown in Fig. 10. According to the roughness measurement results and Eq. (40), the thickness of the discretized element  $t_d$  is in the range from 33 to 52  $\mu\text{m}$ .

The constants of  $K_a$ ,  $K_c$ , and  $K_d$  and the friction coefficients of  $\mu_s$ ,  $\mu_p$ , and  $\mu_c$  in the force model are obtained using the mathematical fitting method. The results of grinding force in the pre-experiments are listed in Table 2. According to the results, the values of  $K_a$ ,  $K_c$ , and  $K_d$  in the theoretical force model are 0.0613,  $6.54 \times 10^3$ , and  $1.49 \times 10^9$ , respectively. The values of  $\mu_s$ ,  $\mu_p$ , and  $\mu_c$  are 0.43, 0.47, and 0.58,

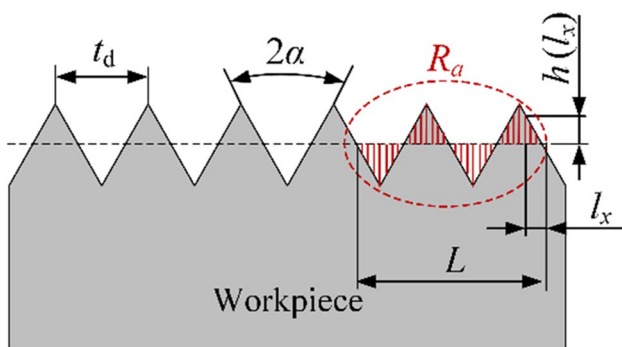


Fig. 10 Illustration of surface roughness and surface contour curve along the y-axis

respectively. The theoretical force model is established, as all values of constants and parameters in the force model are determined.

### 4.2 Intermittent cutting behavior

The intermittent cutting behavior is a characteristic in UVAG. In this section, the grinding trajectories in CG and UVAG are compared at first. Subsequently, the unchanged chip thickness and the quantity of effective grits in UVAG are determined through the theoretical force model.

#### 4.2.1 Contact length between grit and workpiece

In UVAG, the abrasive grits contact to the workpiece, periodically, when the amplitude of ultrasonic vibration is large enough. Fig. 11 shows the grinding trajectories of two adjacent abrasive grits in CG. The two grinding trajectories cannot be directly distinguished in Fig. 11a, because the grinding wheel radius is much larger than the distance between two adjacent abrasive grits. However, it is verified that there is no intersection between the two trajectories through the locally enlarged picture. The distance between the two grinding trajectories is equal to the unchanged chip thickness. The results suggest that the second abrasive grit performs the continuous cutting behaviors without separation.

In UVAG, the difference of two grinding trajectories and the ultrasonic vibration cannot be directly observed, either, due to the magnitude difference, as shown in Fig. 12a. However, some intersections have been found from the locally enlarged figures (Fig. 12b–d). Under the abovementioned conditions, the length of grinding arc is 6.32 mm, the time of abrasive grit passing the grinding arc is  $3.16 \times 10^{-4}$  s, the period of ultrasonic vibration is  $5.18 \times 10^{-5}$  s; therefore, the grit vibrates six times in the grinding arc. The contact length in every vibration period is approximately 0.53 mm. Nevertheless, the actual contact length of a single grit may be smaller than that value, because there are actually more than

Table 2 Grinding force in the pre-experiments

Grinding speed, $v_s$ (m/s)	Worktable feed speed, $v_w$ (mm/min)	Depth of cut, $a_p$ (mm)	Normal force, $F_n$ (N)	Tangential force, $F_t$ (N)
20	150	0.1	344.83	88.63
20	150	0.3	532.95	169.1
20	150	0.5	848.85	248.85
20	250	0.1	422.14	124.37
20	350	0.1	458.85	137.51
25	150	0.1	297.55	66.19
35	150	0.1	248.24	49.60

**Fig. 11** Grinding trajectories in CG. **a** Overall picture. **b** Locally enlarged picture

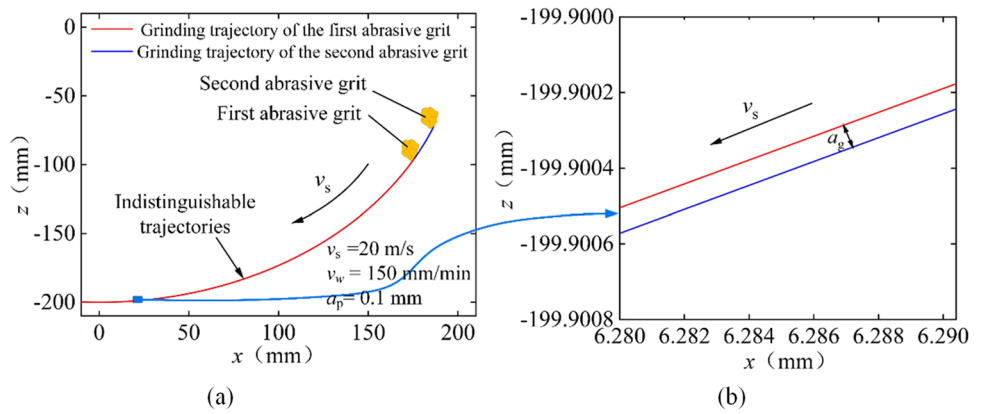
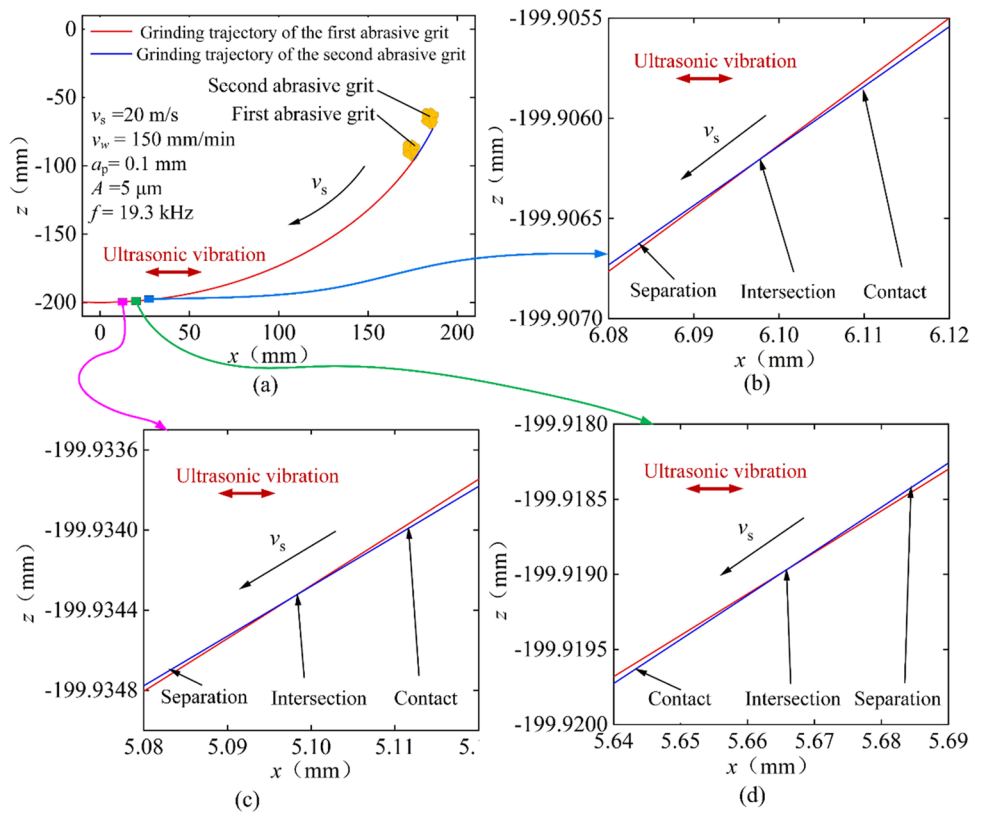


**Fig. 12** Grinding trajectories in UVAG. **a** Overall picture. **b** The first intersection in locally enlarged picture. **c** The third intersection in the locally enlarged picture. **d** The second intersection in the locally enlarged picture



two grit participating in the overlap of grinding trajectories under the current grinding parameters.

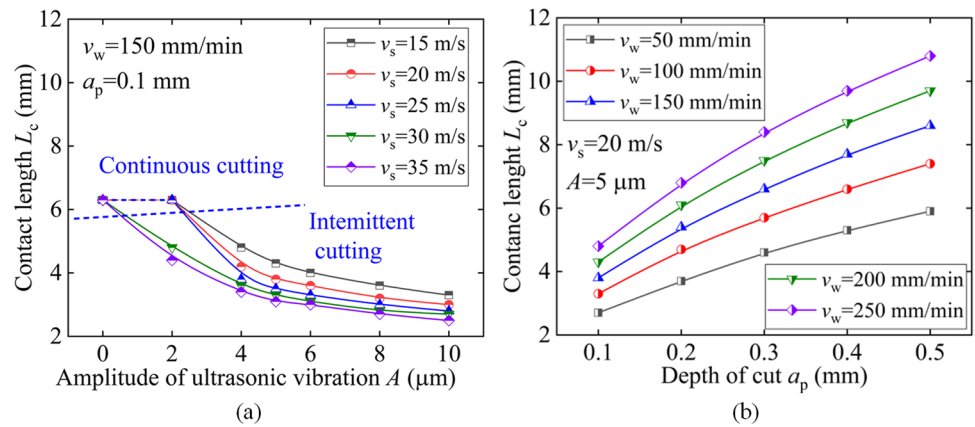
Fig. 13 shows the change in the average contact length of a grit  $L_c$  with the grinding velocity and amplitude of ultrasonic vibration. The contact length is equal to the length of grinding arc when the amplitude of ultrasonic vibration is zero. The contact length decreases from 6.3 to 2.5 mm when the amplitude of ultrasonic vibration and the grinding speed increases to the maximum value of 10  $\mu$ m and 35 m/s, respectively.

In addition, it could be found that the abrasive grits perform the continuous cutting behavior under the conditions of slow grinding velocity (15 m/s), when the vibration

amplitude is small than 2  $\mu$ m. It suggests that the generation of intermittent cutting behavior is conditional, because the increase in grinding velocity would reduce the interval cutting time of adjacent abrasive grits, resulting in more grinding trajectories participating in overlapping. The results indicate that there are five grinding trajectories participating in overlapping when the grinding velocity, worktable feed velocity, and depth of cut are 20 m/s, 150 mm/min, and 0.1 mm. This value is changed to three when the grinding velocity is reduced to 15 m/s.

Fig. 13b displays the influence of worktable feed velocity and depth of cut on the contact length of a grit. Under the condition of 50 mm/min worktable feed speed, the contact length of a

**Fig. 13** Grinding parameters versus contact length of grit. **a** Influence of vibration amplitude and grinding velocity. **b** Influence of cutting depth and worktable feed velocity



grit gradually increases from the 2.7 to 4.8 mm, when the value of  $a_p$  increases from the 0.1 to 0.5 mm. It indicates that the contact length and depth of cut are positively correlated. In terms of the worktable feed speed, the contact length increases from 5.9 mm to the maximum value of 10.8 mm with an increase in the worktable feed velocity from 50 to 250 mm/min.

#### 4.2.2 Quantity of effective grits and unchanged chip thickness

The quantity of effective abrasive grits and the unchanged chip thickness are important factors for the grinding force. However, the difference of grit protrusion height causes the nonuniformity distribution of unchanged chip thickness. The abrasive grits with higher protrusion height should have larger unchanged chip thickness and remove more materials. In UVAG, the intermittent cutting behavior increases the complexity of unchanged chip thickness, because the distribution of unchanged chip thickness should be changed with the vibration phase.

According to grinding trajectory in UVAG, the full vibration phase is a period from 0 to  $2\pi$ , as displayed in Fig. 14a. The tangential ultrasonic vibration can generate vibration components perpendicular to the workpiece surface. Therefore, the full vibration phase includes the contact phase and separation phase. At the separation phase, no abrasive grit could contact to the workpiece. The contact phase is started when more than one grits contact to the workpiece.

Seen from Fig. 14a, the abrasive grit approaches and cuts in the material, when the vibration phase is from 0 to  $0.5\pi$  and from  $1.5$  to  $2\pi$ . The abrasive grit goes away from the material, when the vibration phase changes from  $0.5$  to  $1.5\pi$ . Some of abrasive grits begin contacting to the workpiece material surface at the points of vibration phase  $0.125\pi$  and are about to separate from the workpiece at the phase  $0.875\pi$ . Hence, the contact phase could be considered to start from  $0.125\pi$  and end in  $0.875\pi$ , while the separation phase is from 0 to  $0.125\pi$  and from  $0.875$  to  $2\pi$ , as shown in Fig. 14a.

At the contact phase, the quantity of effective grits and the unchanged chip thickness vary with the vibration phase, as shown in Fig. 14b–d. At the phase of  $0.25\pi$ , the quantity of effective grits decreases with the increase in the unchanged chip thickness, indicating that most of grits are of small unchanged chip thickness. The proportion of grits whose unchanged chip thickness is less than  $0.5\mu\text{m}$ , reaches 73.9%. At this moment, the total quantity of effective grits is 60, and the average unchanged chip thickness of effective grits is  $0.38\mu\text{m}$ . With the vibration phase going to  $0.5\pi$ , the grit vibrates to an extreme position. The distribution of unchanged chip thickness is shown in Fig. 14b. The total quantity of effective grits increases to 232. In this case, the proportion of grits with smaller unchanged chip thickness than  $5\mu\text{m}$  is slightly increases to 77.8% with the steady average unchanged chip thickness of  $0.35\mu\text{m}$ . At the vibration phase of  $0.75\pi$ , the quantity of effective grits is reduced again, because the abrasive grit is about to separate from the workpiece. Only grits with high protrusion height could still cut into the material. The results indicate that the change tendency of effective grit quantity is a dynamic process. It firstly increases and then decreases at the contact phase. The maximum quantity of effective grit is obtained when the vibration phase is equal to an  $0.5\pi$ . At the separation phase, the unchanged chip thickness and quantity of effective grits are always equal to zero.

Fig. 15 shows the change in average unchanged chip thickness with the vibration phase. It can be found that the contact phase approximately lasts from vibration phase of  $0.125$  to  $0.875\pi$  using the current processing parameters. The average unchanged chip thickness reaches the maximum value of  $1.05\mu\text{m}$  at the vibration phase of  $0.125\pi$ . It indicates that a violent impact occurs when the abrasive grit just starts to contact to the workpiece. After the impact, the average unchanged chip thickness decreases quickly to  $0.36\mu\text{m}$ . At that moment, the quantity of effective grits is a quite small value of 4. Subsequently, the quantity of effective grits firstly increases to the maximum value of 232 and then decreases to a small value. Finally,

**Fig. 14** Distribution of unchanged chip thickness versus ultrasonic vibration phase. **a** Vibration phase in the whole period. **b** At the vibration phase of  $0.25\pi$ . **c** At the phase of  $0.5\pi$ . **d** At the phase of  $0.75\pi$

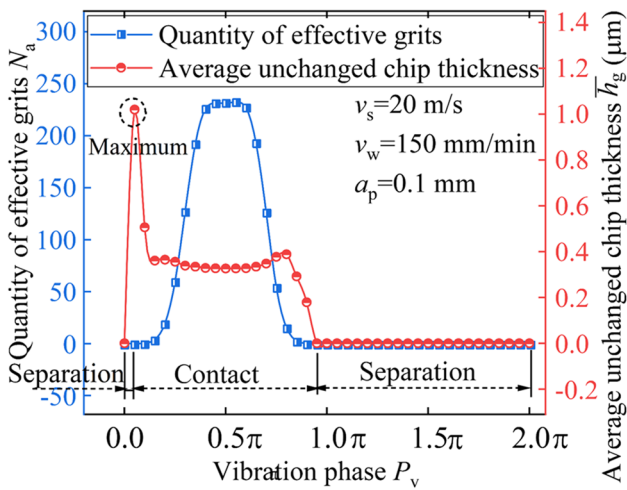
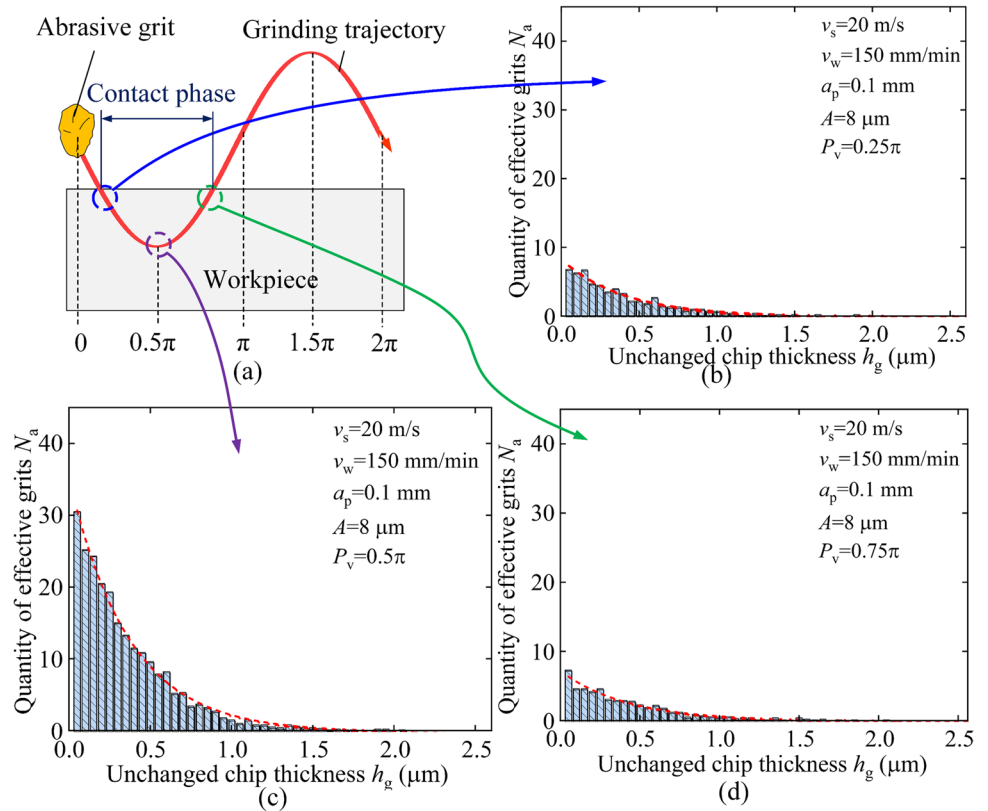


**Fig. 15** Change in the quantity of effective grits and unchanged chip thickness with the vibration phase

all the abrasive grits separate from the workpiece surface; both the unchanged chip thickness and the quantity of effective grits decrease to zero.

### 4.3 Grinding force

Firstly, the influence of vibration phase on the proportion of grits at the three stages is discussed. Then, the force

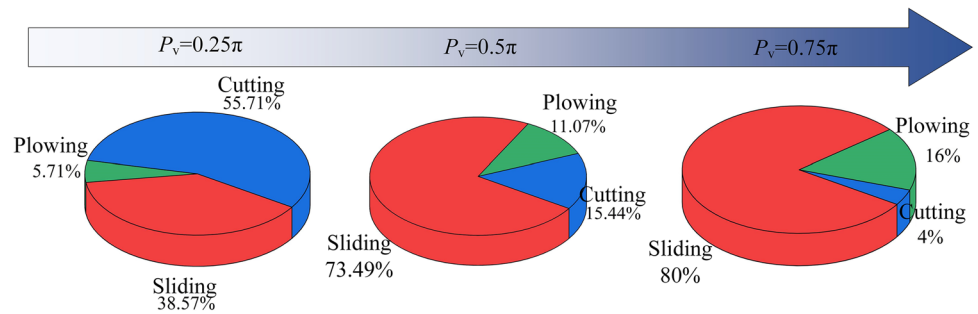
prediction accuracy is verified by comparing the theoretical force value and the experimental results.

#### 4.3.1 Proportion of grits at the three stages

The proportion of grits at the sliding stage, plowing stage and cutting stage is also changed with the vibration phase, as illustrated in Fig. 16. At the vibration phase of  $0.25\pi$ , some abrasive grits just begin contacting to the workpiece surface, the proportion of grits in the cutting stage is 55.71% which is much larger than that in the plowing stage of 5.71% and that in the sliding stage of 38.57%. It is because the direction of vibration speed points to the workpiece surface at this time.

The proportion of grits in the sliding stage increases with the increase in the vibration phase. At the vibration phase of  $0.5\pi$ , the grits vibrate to the extreme position, 73.49% of effective grits in the grinding zone enter the sliding stage. Under this condition, the proportion of grits in the plowing stage is slightly increased to 11.07%. Only 15.44% of effective grits are in the cutting stage. At last, the proportion of grits in the sliding stage sequentially increases to 80% at the vibration phase of  $0.75\pi$ . At this moment, most of effective grits have small unchanged chip thickness when the grinding wheel are about to separate from the workpiece surface.

**Fig. 16** Proportion of grits at the three stages in the contact phase. **a** Proportion of grits at the vibration phase of  $0.25 \pi$ . **b** Proportion of grits at the vibration phase of  $0.5 \pi$ . **c** Proportion of grits at the vibration phase of  $0.75 \pi$



The direction of vibration velocity is a main factor for these phenomena. At the vibration phase of  $0.25 \pi$ , the direction of vibration velocity points to the workpiece surface, which increases the unchanged chip thickness. On the contrary, the direction of vibration speed deviates from the workpiece surface. Therefore, the unchanged chip thickness is reduced, making more grits perform sliding behavior.

### 4.3.2 Force prediction accuracy

The comparison between the theoretical grinding force and the experimental grinding force is shown in Figs. 17 and 18, wherein  $e$  denotes the relative error of

the theoretical model. The normal and tangential grinding forces are 345 N and 89 N, respectively, when the grinding velocity, worktable feed velocity, and depth of cut is 30 m/s, 150 mm/min, and 0.1 mm. In this case, the relative errors are 1.5% in the normal force and 3% in the tangential force. With the increase in the grinding speed to 35 m/s, the normal and tangential grinding forces is reduced to 249 N and 50 N, respectively. On the contrary, the grinding force is increased when the grinding depth and worktable feed speed increases. The grinding forces reach the maximum value of 869 N along the normal direction and 270 N along the tangential direction, when the grinding depth changes to 0.5 mm. In all

**Fig. 17** Prediction error of the theoretical force model for **a** normal grinding force and **b** tangential grinding force

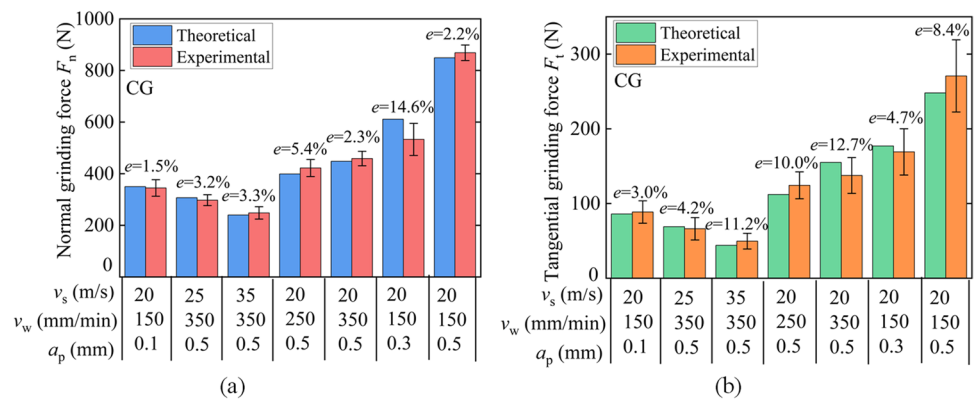
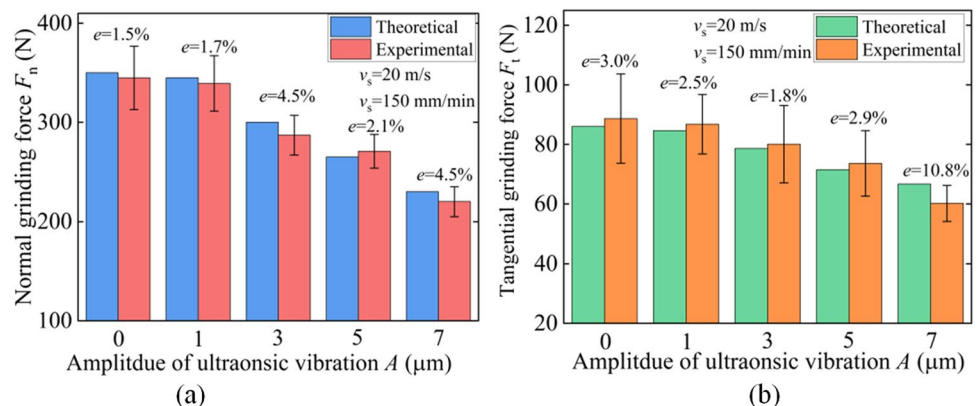


**Fig. 18** Prediction error of the theoretical force model in UVAG for **a** normal grinding force and **b** tangential grinding force



experimental results, the maximum relative error of the theoretical force model is 14.6%, indicating that the force prediction accuracy is smaller than 15%.

Fig. 18 displays the influence of vibration amplitude on the grinding force. The employment of ultrasonic vibration could reduce the grinding force, significantly. The normal grinding force is reduced by maximum 36%, when the vibration amplitude is 7  $\mu\text{m}$ . This phenomenon indicates that the large vibration amplitude promotes the reduction of grinding force, resulting from the small contact length. The proportion of sliding phase and the friction force are reduced. The similar conclusion can be obtained in terms of the tangential grinding force. The force prediction of the model is lower than 10.8%, when the amplitude of ultrasonic vibration is in the range from 0 to 7  $\mu\text{m}$ .

Additionally, it can be found that the grinding forces changes little when the amplitude of ultrasonic vibration changes from 0 to 1  $\mu\text{m}$ . According to the results in Fig. 13a, the intermittent cutting behavior is not happened when the vibration amplitude is very small; therefore, the quantity of effective grits and the unchanged chip thickness are similar as that in CG.

## 5 Conclusions

In the study, the theoretical grinding force model is established for UVAG by determining the number of effective grits and the grinding force of a single grit. Then, the prediction accuracy of theoretical model is verified through the experiments. The main conclusions are submitted as follows:

1. The workpiece surface roughness in all experimental results changes in a small range from 0.47 to 0.75  $\mu\text{m}$ , indicating that the thickness of the discretized element is in the range from 33 to 52  $\mu\text{m}$
2. The unchanged chip thickness and quantity of effective grits are changed with the vibration phase. A large unchanged chip thickness of 1.05  $\mu\text{m}$  is generated at the start of the grits-wheel contact phase. The quantity of effective grits reaches the maximum value of 232 when the grit vibrates to an extreme position in the whole period at the vibration phase of  $0.5\pi$ .
3. Maximum 73.49% of effective grits in the grinding zone are at the cutting stages at the vibration phase of  $0.25\pi$ . This value is reduced to 4% when the grits are about to separate from the workpiece surface at the vibration phases of  $0.75\pi$ . The relative error of the theoretical grinding force model is less than 15%, indicating that the model could be used for grinding force prediction in UVAG.

**Funding** This work was financially supported by the National Natural Science Foundation of China (Nos. 92160301, 92060203, 52175415, and 52205475), Jiangsu Key Laboratory of Precision and Micro-Manufacturing Technology (No. JSKL2223K01), the Science Center for Gas Turbine Project (Nos. P2022-AB-IV-002-001 and P2023-B-IV-003-001), the Natural Science Foundation of Jiangsu Province (No. BK20210295), the Superior Postdoctoral Project of Jiangsu Province (No. 2022ZB215), and the Natural Science Foundation of Henan Province (No. 232300420094).

**Data availability** All data generated or analyzed during this study are included in the present article.

## Declarations

**Ethics approval and consent to participate** The article follows the guidelines of the Committee on Publication Ethics (COPE) and involves no studies on human or animal subjects.

**Consent for publication** Not applicable.

**Competing interests** The authors declare no competing interests.

## References

1. Zhao B, Ding WF, Shan ZD, Wang J, Yao CF, Zhao ZC, Liu J, Xiao SH, Ding Y, Tang XW, Wang XC, Wang YF, Wang X (2023) Collaborative manufacturing technologies of structure shape and surface integrity for complex thin-walled components: status, challenge and tendency. *Chin J Aeronaut* 36(7):1–24
2. Xiao GJ, Zhang YD, Huang Y, Song SY, Chen BQ (2021) Grinding mechanism of titanium alloy: research status and prospect. *J Adv Manuf Sci Technol* 1(1):2020001
3. Gudivada G, Pandey AK (2023) Recent developments in nickel-based superalloys for gas turbine applications: review. *J Alloys Compd* 963:171128
4. Kang KY, Yu GY, Yang WP, Dong JM, Jiang R (2023) Experimental study on creep-feed grinding burn of DD9 nickel-based crystal superalloy. *Diamond Abras Eng* 43(3):355–363
5. Kishore K, Sinha MK, Chauhan SR (2023) A comprehensive investigation of surface morphology during grinding of Inconel 625 using conventional grinding wheels. *J Manuf Process* 97:87–99
6. Bie WB, Zhao B, Chen F, Wang XB, Zhao CY, Niu Y (2023) Progress of ultrasonic vibration-assisted machining surface micro-texture and serviceability. *Diamond Abras Eng* 43(4):401–416
7. Grimmert A, Pachnek F, Wiederkehr P (2023) Temperature modeling of creep-feed grinding processes for nickel-based superalloys with variable heat flux distribution. *CIRP J Manuf Sci Technol* 41:477–489
8. Li BK, Dai CW, Ding WF, Yang CY, Li CH, Kulik O, Shumyacher V (2021) Prediction on grinding force during grinding powder metallurgy nickel-based superalloy FGH96 with electroplated CBN abrasive wheel. *Chin J Aeronaut* 34(8):65–74
9. Wen J, Tang JY, Zhou WH (2021) Study on formation mechanism and regularity of residual stress in ultrasonic vibration grinding of high strength alloy steel. *J Manuf Process* 66:608–622
10. Ni FD, Cong WL (2020) Ultrasonic vibration-assisted (UV-A) manufacturing processes: state of the art and future perspectives. *J Manuf Process* 51:174–190



11. Wang H, Pei ZJ, Cong WL (2020) A feeding-directional cutting force model for end surface grinding of CFRP composites using rotary ultrasonic machining with elliptical ultrasonic vibration. *Int J Mach Tools Manuf* 152:103540
12. Zheng K, Liao WH, Sun LJ, Meng H (2019) Investigation on grinding temperature in ultrasonic vibration-assisted grinding of zirconia ceramics. *Mach Sci Technol* 23(4):612–628
13. Zhou WH, Tang JY, Shao W (2020) Modelling of surface texture and parameters matching considering the interaction of multiple rotation cycles in ultrasonic assisted grinding. *Int J Mech Sci* 166:105246
14. Li DG, Tang JY, Chen HF, Shao W (2019) Study on grinding force model in ultrasonic vibration-assisted grinding of alloy structure steel. *Int J Adv Manuf Technol* 101:1467–1479
15. Yang ZY, Zou P, Zhou L, Wang X (2022) Research on modeling of grinding force in ultrasonic vibration-assisted grinding of 304 stainless steel materials. *Int J Adv Manuf Technol* 120(5–6):3201–3223
16. Li LY, Zhang YB, Cui X, Said Z, Sharma S, Liu MZ, Gao T, Zhou ZM, Wang XM, Li CH (2023) Mechanical behavior and modeling of grinding force: a comparative analysis. *J Manuf Process* 102:921–954
17. Dai CW, Yin Z, Wang P, Miao Q, Chen JJ (2021) Analysis on ground surface in ultrasonic face grinding of silicon carbide (SiC) ceramic with minor vibration amplitude. *Ceram Int* 47(15):21959–21968
18. Liu Q, Chen X, Wang Y, Gindy N (2008) Empirical modelling of grinding force based on multivariate analysis. *J Mater Process* 203(1–3):420–430
19. Fu DK, Ding WF, Miao Q, Xu JH (2017) Simulation research on the grinding forces and stresses distribution in single-grain surface grinding of Ti-6Al-4V alloy when considering the actual cutting-depth variation. *Int J Adv Manuf Technol* 91(9–12):3591–3602
20. Fu DK, Ding WF, Yang SB, Miao Q, Fu YC (2017) Formation mechanism and geometry characteristics of exit-direction burrs generated in surface grinding of Ti-6Al-4V titanium alloy. *Int J Adv Manuf Technol* 89(5–8):2299–2313
21. Yin L, Zhao B, Huo BJ, Bie WB, Zhao CY (2021) Analytical modeling of grinding force and experimental study on ultrasonic-assisted forming grinding gear. *Int J Adv Manuf Technol* 114:3657–3673
22. Sun JG, Li CH, Zhou ZM, Liu B, Zhang YB, Yang M, Gao T, Liu MZ, Cui X, Li BK, Li RZ, Dambatta YS, Sharma S (2023) Material removal mechanism and force modeling in ultrasonic vibration-assisted micro-grinding biological bone. *Chin J Mech Eng* 36:129
23. Jamshidi A, Gurtan M, Budak E (2019) Identification of active number of grits and its effects on mechanics and dynamics of abrasive processes. *J Mater Process Technol* 273:116239
24. Hou ZB, Komanduri R (2003) On the mechanics of the grinding process – part I. Stochastic nature of the grinding process. *Int J Mach Tools Manuf* 43(15):1579–1593
25. Liu MZ, Li CH, Zhang YB, Yang M, Gao T, Cui X, Wang XM, Xu WH, Zhou ZM, Liu B, Said Z, Li RZ, Sharma S (2023) Analysis of grinding mechanics and improved grinding force model based on randomized grain geometric characteristics. *Chin J Aeronaut* 36(7):160–193
26. Yang M, Li CH, Zhang YB, Jia DZ, Li RZ, Hou YL, Cao HJ, Wang J (2019) Predictive model for minimum chip thickness and size effect in single diamond grain grinding of zirconia ceramics under different lubricating conditions. *Ceram Int* 45(12):14908–14920
27. Zhang WJ, Gong YD, Zhao XL, Xu YC, Li X, Yin GQ, Zhao JB (2023) Modeling and analysis of tangential force in robot abrasive belt grinding of nickel-based superalloy. *Arch Civ Mech Eng* 23(2):124
28. Wu H, Yao ZQ (2021) Force modeling for 2D freeform grinding with infinitesimal method. *J Manuf Process* 70:108–120
29. Cai SJ, Yao B, Zhang Q, Cai ZQ, Feng W, Chen BQ, He Z (2020) Dynamic grinding force model for carbide insert peripheral grinding based on grain element method. *J Manuf Process* 58:1200–1210
30. Yang ZC, Zhu LD, Zhang GX, Ni CB, Lin B (2020) Review of ultrasonic vibration-assisted machining in advanced materials. *Int J Mach Tools Manuf* 156:103594
31. Jamshidi H, Budak E (2020) An analytical grinding force model based on individual grit interaction. *J Mater Process Technol* 283:116700
32. Wang QY, Liang ZQ, Wang XB, Bai SW, Yeo SH, Jia S (2020) Modelling and analysis of generation mechanism of micro-surface topography during elliptical ultrasonic assisted grinding. *J Mater Process Technol* 279:116585
33. Yang ZC, Zhu LD, Lin B, Zhang GX, Ni CB, Sui TY (2019) The grinding force modeling and experimental study of ZrO<sub>2</sub> ceramic materials in ultrasonic vibration assisted grinding. *Ceram Int* 45(7):8873–8889
34. Cao Y, Zhao B, Ding WF, Liu YC, Wang LF (2021) On the tool wear behavior during ultrasonic vibration-assisted form grinding with alumina wheels. *Ceram Int* 47(18):26465–26474
35. Durgumahanti USP, Singhn Rao PV (2010) A new model for grinding force prediction and analysis. *Int J Mach Tools Manuf* 50(3):231–240
36. Lu SX, Gao H, Bao YJ, Xu QH (2019) A model for force prediction in grinding holes of SiC<sub>p</sub>/Al composites. *Int J Mech Sci* 160:1–14
37. Yang M, Li CH, Zhang YB, Jia DZ, Zhang XP, Hou YL, Li RZ, Wang J (2017) Maximum undeformed equivalent chip thickness for ductile-brittle transition of zirconia ceramics under different lubrication conditions. *Int J Mach Tools Manuf* 122:55–65
38. Adibi H, Jamaati F, Rahimi A (2022) Analytical simulation of grinding force based on the micro-mechanisms of cutting between grain-workpiece. *Int J Adv Manuf Technol* 119(7–8):4181–4801
39. Cha E, Bogy DB (1995) Numerical simulations of slider interaction with multiple asperity using Hertzian contact model. *J Tribol - Trans ASME* 117(4):575–579
40. Wang DX, Ge PQ, Bie WB, Jiang JL (2014) Grain trajectory and grain workpiece contact analyses for modeling of grinding force and energy partition. *Int J Adv Manuf Technol* 70(9–12):2111–2123
41. Vathaire MD, Delamare F, Felder E (1981) An upper bound model of ploughing by a pyramidal indenter. *Wear* 66:55–64
42. Azarkhin A, Richmond O (1992) A model of ploughing by a pyramidal indenter - upper bound method for stress-free surfaces. *Wear* 157:409–418
43. Ozlu E, Molinari A, Budak E (2010) Two-zone analytical contact model applied to orthogonal cutting. *Mach Sci Technol* 14:323–343
44. Mitrofanov AV, Ahmed N, Babitsky VI, Silberschmidt VV (2005) Effect of lubrication and cutting parameters on ultrasonically assisted turning of Inconel 718. *J Mater Process Technol* 162:649–654
45. Li DG, Tang JY, Chen HF, Shao W (2019) Study on grinding force model in ultrasonic vibration-assisted grinding of alloy structural steel. *Int J Adv Manuf Technol* 101(5–8):1467–1479
46. Jiang JL, Ge PQ, Sun SF, Wang DX, Wang DL, Yang Y (2016) From the microscopic interaction mechanism to the grinding

- temperature field: an integrated modelling on the grinding process. *Int J Mach Tools Manuf* 110:27–42
47. Egashira K, Kumagai R, Okina R, Yamaguchi K, Ota M (2004) Drilling of microholes down to 10  $\mu\text{m}$  in diameter using ultrasonic grinding. *Precis Eng* 38(3):605–610
  48. Tang JY, Du J, Chen YB (2009) Modeling and experimental study of grinding forces in surface grinding. *J Mater Process Technol* 209(6):2847–2854
  49. Cao Y, Zhao B, Ding WF, Huang Q (2023) Vibration characteristics and machining performance of a novel perforated ultrasonic vibration platform in the grinding of particulate-reinforced titanium matrix composites. *Front Mech Eng* 18(1):14
  50. Cao Y, Zhu YJ, Ding WF, Qiu YT, Wang LF, Xu JH (2022) Vibration coupling effects and machining behavior of ultrasonic vibration plate device for creep-feed grinding of Inconel 718 nickel-based superalloy. *Chin J Aeronaut* 35(2):332–345
  51. Han L, Kang RK, Zhang Y, Dong ZG, Bao Y (2021) Research on surface integrity of GH4169 machined by ultrasonic assisted grinding. *Diamond Abras Eng* 41(5):46–51

**Publisher's note** Springer Nature remains neutral with regard to jurisdictional claims in published maps and institutional affiliations.

Springer Nature or its licensor (e.g. a society or other partner) holds exclusive rights to this article under a publishing agreement with the author(s) or other rightsholder(s); author self-archiving of the accepted manuscript version of this article is solely governed by the terms of such publishing agreement and applicable law.